

## PAPER



Cite this: *Dalton Trans.*, 2020, **49**, 12854

# Increase of network hydrophilicity from *sql* to *lvt* supramolecular isomers of Cu-MOFs with the bifunctional 4-(3,5-dimethyl-1*H*-pyrazol-4-yl)benzoate linker†

Saskia Menzel,  Simon Millan,  Simon-Patrick Höfert, Alexander Nuhnen, Serkan Gökpinar, Alexa Schmitz and Christoph Janiak \*

The bifunctional linker 4-(3,5-dimethyl-1*H*-pyrazol-4-yl)benzoic acid (*H*<sub>2</sub>mpba) was used for the synthesis of new (square lattice) **sql** 2D metal–organic frameworks (MOFs) [Cu(*H*mpba)<sub>2</sub>]-L (L = DMF or ACN) in a solvent-mixture of dimethylformamide/water and acetonitrile/water. These **sql** 2D MOFs are supramolecular isomers of the **lvt** 3D network [Cu(*H*mpba)<sub>2</sub>]-4MeOH·1H<sub>2</sub>O (**lvt**-MeOH) that was synthesized previously by Richardson and co-workers. All these frameworks are potentially porous structures with solvent molecules included in the channels of the as synthesized materials. After activation all three materials showed good CO<sub>2</sub> adsorption capacity, demonstrated here for **lvt**-MeOH for the first time, with a saturation uptake of 113 cm<sup>3</sup> g<sup>-1</sup> (**lvt**-MeOH-act.), 111 cm<sup>3</sup> g<sup>-1</sup> (**sql**-DMF-act.) and 90 cm<sup>3</sup> g<sup>-1</sup> (**sql**-ACN-act.) at 195 K. The flexibility of the **lvt**-MeOH-act. network is evidenced by a gate-opening effect seen in the CO<sub>2</sub> measurement at 195 K and under gravimetric high-pressure CO<sub>2</sub> adsorption. According to the water and ethanol sorption measurements the new **sql** frameworks can be categorized as hydrophobic materials in contrast to the hydrophilic **lvt** framework. In the **lvt**-MeOH structure the crystal solvent can be replaced with water to yield the structurally authenticated water-only network **lvt**-H<sub>2</sub>O containing 3D arrays of S<sub>4</sub>-symmetric (H<sub>2</sub>O)<sub>20</sub> clusters.

Received 27th July 2020,  
Accepted 2nd September 2020

DOI: 10.1039/d0dt02642e

rsc.li/dalton

## Introduction

New ligand classes are still important for the progress of metal–organic frameworks (MOFs).<sup>1</sup> For example, the ligand donor group is crucial to increasing MOF stability and/or to tune the MOF structure for potential applications in gas storage/separation,<sup>2</sup> catalysis,<sup>3</sup> optics,<sup>4</sup> magnetism,<sup>5</sup> sensing,<sup>6</sup> biomedicine<sup>7</sup> or as porous fillers in mixed-matrix membranes.<sup>8,9</sup>

In MOFs, the usage of mixed-ligand systems of different functionality is common, for example dicarboxylates are combined with bipyridines<sup>10</sup> or bipyrazoles.<sup>11,12</sup> This led to the evolution of bifunctional (also termed heteroditopic) ligands like pyridine-carboxylates,<sup>13,14</sup> phosphonate-carboxylates,<sup>15,16</sup> pyrazolate-carboxylates,<sup>17,18</sup> or pyrazolate-phosphonates.<sup>19</sup> Bifunctional doubly-deprotonated pyrazolate-carboxylate ligands have specifically been employed to synthesize more

stable versions of their dicarboxylate analogs due to the greater covalency of the metal-pyrazolate bond compared to metal carboxylate bond.

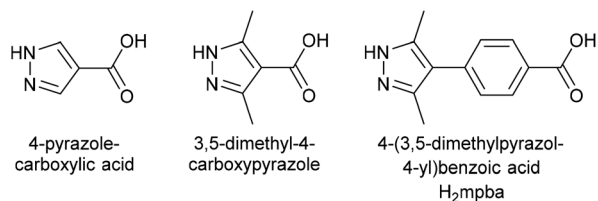
The introduction of linkers with donor groups of stronger basicity such as imidazolates or pyrazolates can thus contribute to markedly increase the stability of MOFs toward water. In metal-azolate frameworks (MAFs), including zeolitic-imidazolate frameworks (ZIFs), the metal centers are coordinated by linkers from imidazolate, pyrazolate, triazolate or tetrazolate derivatives. MAFs can show high thermal and chemical stability. In addition, the substituents of the azolate linkers could efficiently tune the hydrophobicity of the framework, contributing to higher kinetic stability against water.<sup>8,9</sup>

MOFs with bifunctional pyrazole-carboxylic acid linkers (Scheme 1) have been utilized to capture nerve gas agents,<sup>17</sup> as hydrophobic materials for solid-phase extraction,<sup>20</sup> to synthesize MOFs with ordered vacancies<sup>21</sup> and incorporated into mixed-matrix-membranes.<sup>8,9</sup> If the pyrazole group is not deprotonated during the MOF formation then the pyrazole-carboxylate linker mimics a pyridine-carboxylate linker with the adjacent NH-function as an additional interaction site.<sup>17,18,20–24</sup>

The combination of a carboxylate and a pyrazole group in one ligand can give different topological networks based on

*Institut für Anorganische Chemie und Strukturchemie, Heinrich-Heine Universität Düsseldorf, 40204 Düsseldorf, Germany. E-mail: janiak@hhu.de*

† Electronic supplementary information (ESI) available: IR, PXRD, crystal data, TGA, NMR, gas sorption, porosity, heat of adsorption. CCDC 1999766–1999768. For ESI and crystallographic data in CIF or other electronic format see DOI: 10.1039/d0dt02642e



**Scheme 1** Bifunctional pyrazole-carboxylic acid linkers reported in the literature and the 4-(3,5-dimethyl-1*H*-pyrazol-4-yl)benzoic acid linker,  $H_2mpba$  used in this work.

the same building blocks upon variation of the synthesis conditions.<sup>25</sup> Generally, the product in a MOF-synthesis can vary with solvent,<sup>26,29,31</sup> temperature,<sup>27,28</sup> the metal salt to ligand ratio, the metal counterions and additives.<sup>28</sup> This phenomenon can be exemplified through the three isolated solvent-dependent supramolecular isomers with **dia**-topology (**dia** = diamond net) of  $[Zn(Hmpba)_2] \cdot L_{solv}$  with  $L_{solv}$  = dioxane,<sup>29</sup> ethanol/water,<sup>29</sup> DMF/water,<sup>22</sup> methanol/water<sup>22</sup> and guest-free (non-porous) by using pure water as solvent.<sup>29</sup> In addition, a supramolecular isomer with **afw**-topology<sup>30</sup> based on the identical tetrahedrally coordinated zinc-knots, but with larger porosity has been synthesized by using toluene as a templating solvent.<sup>31</sup>

Besides the arrangement of the same building blocks in the supramolecular isomers with different net topologies, changes in the reaction conditions can also yield a different packing of nets with overall same topologies guided by weak supramolecular interactions.<sup>32</sup>

The occurrence of such supramolecular isomers can be an opportunity for better understanding the factors which influence nucleation and crystal growth, because at the moment little is known on the controlling factors of such supramolecular isomers, except that the probability for the formation of supramolecular isomers increases in structures with flexible parts and ligands with functional groups that can form hydrogen bonds.<sup>28</sup>

Herein, we report the 2D nets **sql**- $[Cu(Hmpba)_2] \cdot xDMF$  and **sql**- $[Cu(Hmpba)_2] \cdot 2ACN$ , which are two crystallographically distinct supramolecular isomers to the known 3D net **lvt**- $[Cu(Hmpba)_2] \cdot 4MeOH \cdot 1H_2O$  (**lvt**-MeOH), synthesized by Richardson and co-workers (**lvt** is a  $4^2 \cdot 8^4$  net<sup>30</sup>).<sup>22</sup> We examined both supramolecular isomers regarding their vapor and gas sorption properties, thereby highlighting the seemingly important role of the N-H donor function of the pyrazole-moiety. In addition, we were able to obtain a 3D **lvt**- $H_2O$  net by replacing the solvent in **lvt**-MeOH with water.

## Experimental

### Materials and methods

Reagents were obtained from commercial sources and used as received without further purification:  $Cu(NO_3)_2 \cdot 2.5H_2O$  (99%+, Alfa Aesar),  $CuSO_4 \cdot 5H_2O$  (99%+, Alfa Aesar), acetonitrile,

methanol, *N,N*-dimethylformamide (ACS grade, VWR), de-ionized water (DI). The synthesis of 4-(3,5-dimethyl-1*H*-pyrazol-4-yl)benzoic acid ( $H_2mpba$ ), was carried out according to the literature procedure.<sup>22</sup>

Elemental analyses (CHN) were performed using a PerkinElmer 2400 series II elemental analyzer. IR-spectra were recorded on a Bruker FT-IR Tensor 37 spectrometer in the 4000–500  $cm^{-1}$  region with 2  $cm^{-1}$  resolution as KBr disks. Thermogravimetric analysis (TGA) was performed using a Netzsch TG 209 F3 Tarsus from 20 to 600 °C with a heating range of 5 K  $min^{-1}$  under nitrogen atmosphere. <sup>1</sup>H NMR spectra were measured with a Bruker Avance III-300. The powder X-ray diffraction (PXRD) measurements were carried out on samples at ambient temperature with a Bruker D2 Phaser powder diffractometer using a flat silicon, low-background sample holder at 30 kV, 10 mA (100 W) for Cu-K $\alpha$  radiation ( $\lambda = 1.54184 \text{ \AA}$ ). In all diffractograms, the most intense reflection was normalized to 1. Simulated powder X-ray diffractograms were obtained from single-crystal data using the MERCURY 3.5.1 software programme.<sup>33</sup> Gas sorption measurements up to one bar were performed on an ASAP 2020 automatic sorption analyzer (Micromeritics). High-pressure gravimetric adsorption of  $CO_2$  was conducted on a RUBOTHERM (IsoSORB) STATIC and the mass change was measured with a magnetic suspension balance (resolution 0.01 mg; reproducibility, *i.e.* standard deviation 0.03 mg) between 0–20 bar. Water and ethanol sorption measurements were carried out on a VSTAR<sup>TM</sup> sorption analyzer (Model number Vstar4-0000-1000-XS) from Quantachrome. The gas sorption experiments and the liquid sorption measurements were performed on sample amounts of at least 30 mg, which were degassed on the ASAP 2020 at 160 °C for 8 h (**sql**-DMF and **lvt**-MeOH) and at 110 °C for 3 h (**sql**-ACN).  $N_2$  sorption measurements were carried out at 77 K,  $CO_2$  at 293 K, 273 K (ice/deionized water) and 195 K (acetone/dry ice bath) and  $CH_4$  at 293 K and 273 K.

### X-ray crystallography

Suitable single crystals were carefully selected under a polarized-light microscope and mounted in a perfluorinated oil drop. The single-crystal diffraction data was collected using a Bruker Kappa APEX2 Duo CCD diffractometer with a microfocus source for Mo-K $\alpha$  radiation ( $\lambda = 0.71073 \text{ \AA}$ ) and multi-layer mirror monochromator. The data were collected under a cold nitrogen gas-stream at  $140 \pm 2$  K using the APEX2 software<sup>34</sup> for unit-cell determination and data collection. Data reduction was performed by SAINT 8.34A (integration) and SADABS (empirical absorption correction).<sup>35</sup> The structures were solved by direct methods using SHELXT-2015.<sup>36</sup> Full-matrix least squares refinements on  $F^2$  were carried out with SHELXL-2017/1. All non-hydrogen atoms were refined with anisotropic temperature factors. Hydrogen atoms for aromatic and aliphatic CH and  $CH_3$  groups were positioned geometrically ( $C-H = 0.95 \text{ \AA}$  for CH and  $0.98 \text{ \AA}$  for  $CH_3$ ) and refined using a riding model (AFIX 43 for CH and AFIX 137 for  $CH_3$ ), with  $U_{iso}(H) = 1.2U_{eq}(CH)$  and  $U_{iso}(H) = 1.5U_{eq}(CH_3)$ . The hydrogen atoms of

the NH group were positioned and refined freely with  $U_{\text{iso}}(\text{H}) = 1.5U_{\text{eq}}(\text{N})$ .

The hydrogen atoms of the solvent water molecules were found and refined freely with  $U_{\text{iso}}(\text{H}) = 1.5U_{\text{eq}}(\text{O})$  and restrained using DFIX with  $d = 0.82$  and DANG with  $d = 1.3$ .

For **sql**-[Cu(Hmpba)<sub>2</sub>]<sub>2</sub>·xDMF (**sql**-DMF) one DMF molecule was found and refined with full occupancy. Disordered solvent molecules resulting in non-refinable electron density were removed *via* the SQUEEZE command in PLATON.<sup>37</sup> The resulting solvent accessible volume of 404 Å<sup>3</sup> per unit cell contained 88 electrons, which would correspond to 2DMF molecules (40 e each) or 0.5DMF for the given asymmetric formula unit ( $Z = 4$ ). For **sql**-[Cu(Hmpba)<sub>2</sub>]<sub>2</sub>·2ACN (**sql**-ACN) two ACN molecules were refined with full occupancy. For **lvt**-[Cu(Hmpba)<sub>2</sub>]<sub>2</sub>·9H<sub>2</sub>O (**lvt**-H<sub>2</sub>O) H<sub>2</sub>O molecules were found with refined site occupancy factors ranging from 0.858 to 0.963 resulting in a total of 8.97 H<sub>2</sub>O molecules.

Crystallographic and refinement details are collected in Table S1, ESI.† The structural data have been deposited with the Cambridge Crystallographic Data Center under deposition numbers CCDC 1999766–1999768.† The supramolecular packing interactions have been analyzed with PLATON.<sup>37</sup>

### Synthetic procedures

[Cu(Hmpba)<sub>2</sub>]<sub>2</sub>·xDMF (**sql**-DMF,  $x = 1$ –1.5). A solution of H<sub>2</sub>mpba (20 mg, 0.092 mmol) and of Cu(NO<sub>3</sub>)<sub>2</sub>·2.5H<sub>2</sub>O (11 mg, 0.047 mmol) in *N,N*-dimethylformamide (DMF, 1.65 mL) and deionized water (0.15 mL) was sealed in a glass vial with screw cap and heated at 60 °C for three days after which deep blue star-shaped crystal clusters with single thin needles had formed and were collected after cooling to room temperature (yield 21 mg, 79%, based on the metal salt and one DMF molecule in the product). Calc. for C<sub>27</sub>H<sub>29</sub>CuN<sub>5</sub>O<sub>5</sub> ( $x = 1$ , 567.10 g mol<sup>-1</sup>) C 57.18, H 5.15, N 12.35, for C<sub>28.5</sub>H<sub>32.5</sub>CuN<sub>5.5</sub>O<sub>5.5</sub> ( $x = 1.5$ , 603.64 g mol<sup>-1</sup>) C 56.71, H 5.43, N 12.76; found C 55.94, H 5.58, N 12.42%.

[Cu(Hmpba)<sub>2</sub>]<sub>2</sub>·2ACN (**sql**-ACN). A solution of H<sub>2</sub>mpba (20 mg 0.092 mmol) and of Cu(NO<sub>3</sub>)<sub>2</sub>·2.5H<sub>2</sub>O (11 mg 0.047 mmol) in acetonitrile (ACN, 1.65 mL) and deionized water (1.15 mL) were sealed in a glass vial with screw cap and heated at 80 °C for three days after which deep violet needle-shape crystals had formed (yield 20 mg, 72%, based on the metal salt). Calc. for C<sub>28</sub>H<sub>28</sub>CuN<sub>6</sub>O<sub>4</sub> (2ACN, 576.10 g mol<sup>-1</sup>) C 58.37, H 4.90, N 14.59; found C 58.35, H 4.81, N 13.87%.

[Cu(Hmpba)<sub>2</sub>]<sub>2</sub>·4MeOH·1H<sub>2</sub>O (**lvt**-MeOH) was synthesized as described by Richardson and co-workers.<sup>22</sup>

[Cu(Hmpba)<sub>2</sub>]<sub>2</sub>·9H<sub>2</sub>O (**lvt**-H<sub>2</sub>O) was synthesized by exchanging the methanol in **lvt**-MeOH against water. The methanol was removed with a pipette and the crystals placed on filter paper for brief (5 min) air drying. After this the crystals of **lvt**-MeOH (44 mg) were put in DI water (13 mL) at room temperature. During the first fourteen days, the DI water was replaced twice a day (removal with a pipette) to allow the softest exchange as possible to maintain the crystal quality. During the next seven days, the solvent exchange was continued at 40 °C and the DI water was replaced once a day. After 21 days

bright violet crystals were collected (yield 38 mg, 86%). Calc. for C<sub>24</sub>H<sub>40</sub>CuN<sub>4</sub>O<sub>13</sub> (9H<sub>2</sub>O, 656.15 g mol<sup>-1</sup>) C 43.93, H 6.14, N 8.54; found C 43.85, H 6.81, N 8.11%.

## Results and discussion

### Crystal structures of **sql**-DMF and **sql**-ACN

Deep blue star-shaped crystal clusters with single thin needles of [Cu(Hmpba)<sub>2</sub>]<sub>2</sub>·xDMF, denoted as **sql**-DMF and violet needle-shaped crystals of [Cu(Hmpba)<sub>2</sub>]<sub>2</sub>·2ACN (**sql**-ACN) were obtained from Cu(NO<sub>3</sub>)<sub>2</sub>·2.5H<sub>2</sub>O and H<sub>2</sub>mpba in the solvent mixtures of DMF/H<sub>2</sub>O or ACN/H<sub>2</sub>O, respectively (see the images of the crystalline phases in Fig. S3, ESI†). The phase purity was ascertained by PXRD (Fig. S1a, ESI†). The compound **sql**-DMF crystallizes in the monoclinic space group  $P2_1/n$ . The asymmetric unit contains one Cu(II) atom, two monodeprotonated ligands Hmpba<sup>-</sup> and one DMF solvent molecule of crystallization (Fig. 1). Each copper ion is surrounded square-planar by two *trans* carboxylate-oxygen atoms and two *trans* pyrazole-nitrogen atoms from four different ligands representing the 4-*c* square {CuN<sub>2</sub>O<sub>2</sub>}-nodes of a two-dimensional **sql**-framework. The Cu–O and Cu–N bond lengths lie between 1.950(5)–1.970(4) Å and 1.980(5)–1.985(5) Å, respectively.

The compound **sql**-ACN crystallizes in the monoclinic space group  $P2_1/c$ . The asymmetric unit contains two Cu(II) ions with a symmetry induced site-occupancy-factor of 0.5, two monodeprotonated Hmpba<sup>-</sup> ligands and two disordered ACN molecules, representing two independent building units or a  $Z' = 2$  structure (Fig. S4b, ESI†). The coordination environment of the two copper ions is also square planar, with *trans*-O and *trans*-N coordination and with Cu–O and Cu–N bond lengths between 1.937(8)–1.953(8) Å and 1.961(0)–1.998(5) Å, respectively. The two crystallographically distinct

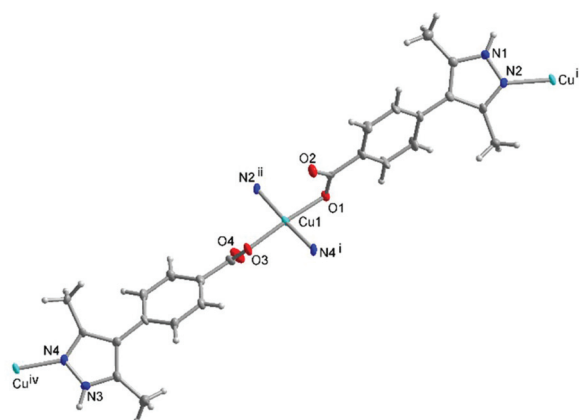


**Fig. 1** Metal–ligand coordination in [Cu(Hmpba)<sub>2</sub>]<sub>2</sub>·xDMF (**sql**-DMF) (70% thermal ellipsoids). Symmetry transformations: i =  $x + 1/2, -y + 3/2, z + 1/2$ ; ii =  $x - 1/2, -y + 1/2, z - 1/2$ ; iii =  $x + 1/2, -y + 1/2, z + 1/2$ ; iv =  $x - 1/2, -y + 3/2, z - 1/2$ . The DMF solvent molecule is omitted for clarity (see Fig. S4a†). The essentially identical metal–ligand coordination for **sql**-ACN is shown in Fig. S4b, ESI.†

copper ions are the 4-c square  $\{\text{CuN}_2\text{O}_2\}$ -nodes of two independent **sql**-networks.

Because of the structural similarity and for the better highlight of their structural differences, the supramolecular features of **sql**-DMF and **sql**-ACN are discussed together. The most important supramolecular interactions in both compounds are interlayer  $\text{NH}\cdots\text{O}$  hydrogen bonds from the NH function to an oxygen atom of a carboxylate group and  $\text{CH}\cdots\pi$  interactions<sup>38</sup> between the phenyl-rings of adjacent layers (Fig. 7).

By these interlayer  $\text{NH}\cdots\text{O}$  hydrogen bonds and  $\text{C-H}\cdots\pi$  interactions, the layers in both **sql**-DMF and **sql**-ACN are

arranged in an eclipsed fashion with formation of a potentially porous supramolecular network with channels along the *a* direction (Fig. 2). The channels have a lozenge shape with diagonals of 6.3 Å and 6.8 Å in **sql**-DMF and of 5.0 Å and 6.2 Å in **sql**-ACN with the van der Waals surface taken into account (Fig. 2). The stacking sequence for **sql**-DMF is AA' because adjacent layers are related by an inversion symmetry operation. In the **sql**-ACN structure the two crystallographically independent networks yield an eclipsed AB sequence. The networks **sql**-DMF and **sql**-ACN can be interpreted as packing polymorphs.<sup>39,40</sup> The role of the DMF and ACN solvent of crystallization is attributed to a templating effect together with an

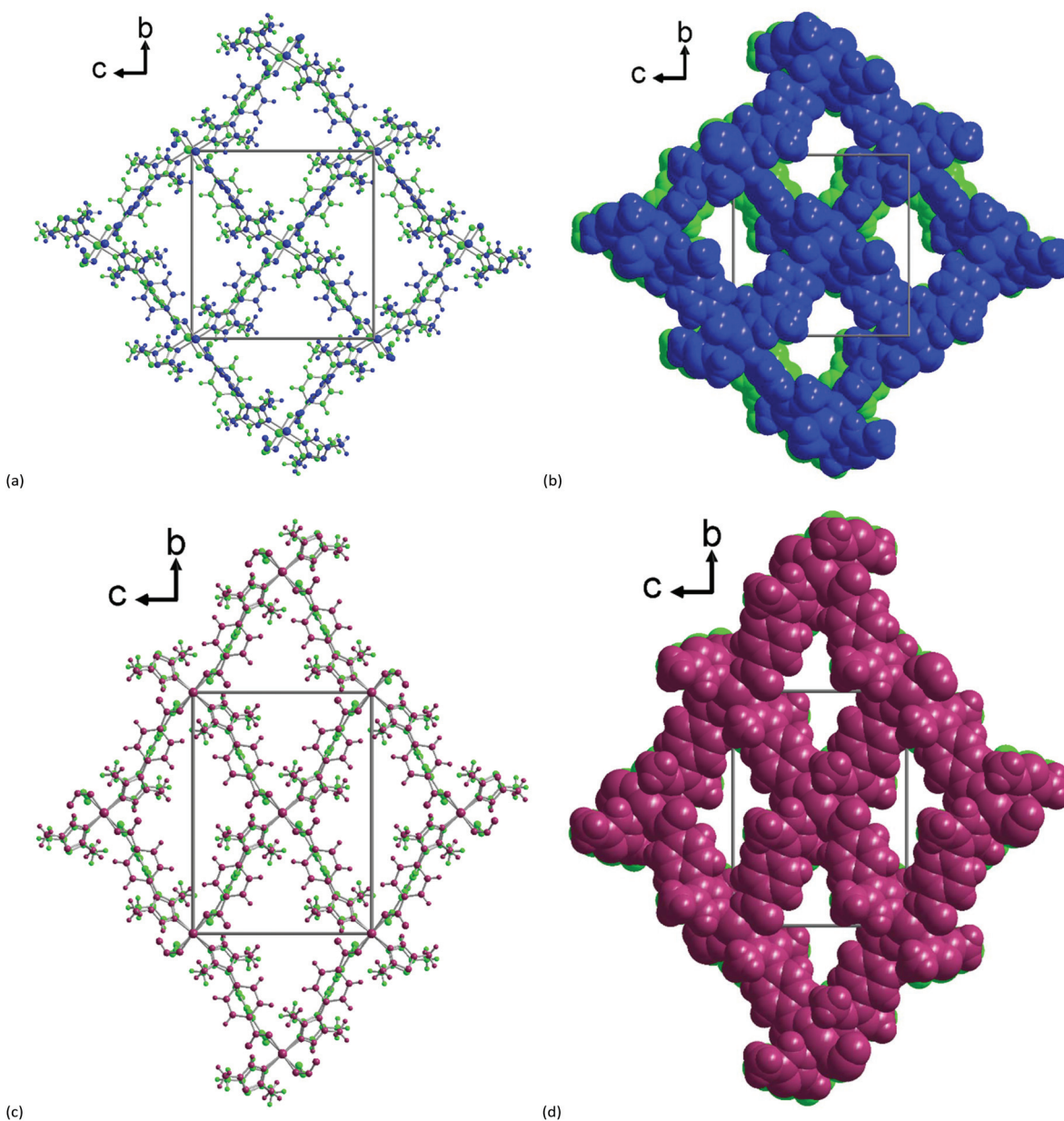


**Fig. 2** Top row: Inversion-symmetric AA' stacking of the nets along the *a* direction in **sql**-DMF in (a) ball-and-stick and (b) space-filling presentation. Bottom row: AB stacking of two symmetry-independent A and B nets along *a* in **sql**-ACN in (c) ball-and-stick and (d) space-filling presentation. The two nets are represented in different color for clarity.

influence on the linker conformation in form of weak interactions.<sup>32</sup> The solvent is obviously the controlling parameter for the crystallization.

### Crystal structure of *lvt*-H<sub>2</sub>O

In order to obtain a structure of [Cu(Hmpba)<sub>2</sub>] with water as the only guest molecule, we replaced the methanol in (*lvt*-MeOH)<sup>22</sup> by water. A direct synthesis was not possible when water was attempted to be used as the only solvent during the synthesis. The solvent exchange from *lvt*-MeOH to [Cu(Hmpba)<sub>2</sub>] $\cdot$ 9H<sub>2</sub>O (*lvt*-H<sub>2</sub>O) was verified by a single-crystal X-ray structure and NMR spectroscopy (absence of MeOH, see Fig. S11, ESI<sup>†</sup>). In the structure of *lvt*-H<sub>2</sub>O all five symmetry independent water molecules with their hydrogen atoms were found and refined. The diffractogram collected after 14 days matches the simulation based on the single crystal analysis of *lvt*-H<sub>2</sub>O (Fig. 3) and is distinctively different from *lvt*-MeOH, although a small contribution *lvt*-MeOH cannot be fully ruled out. When the solvent exchange was prolonged to 21 days the crystallinity seemed to deteriorate as evidenced by a lower reflection intensity (Fig. S1b, ESI<sup>†</sup>)

The all-water structure, *lvt*-H<sub>2</sub>O, is of interest in the context of cycling water sorption of MOF for heat transformation.<sup>41–44</sup> The compounds *lvt*-MeOH and *lvt*-H<sub>2</sub>O are isostructural and crystallize in the *I*4<sub>1</sub>/*a* tetragonal space group with very similar cell parameters. The 3D framework *lvt*-H<sub>2</sub>O, just as *lvt*-MeOH yields a triply interpenetrated structure (Fig. S5 ESI<sup>†</sup>). The copper atom has a centrosymmetric *trans*-{CuN<sub>2</sub>O<sub>4</sub>} environment. Two carboxylate groups form a short (1.942 Å) and a Jahn–Teller-distorted long (2.727 Å) Cu–O bond giving a tetragonally elongated or square-bipyramidal coordination environment for the copper atom (Fig. 4a). The NH donor function of the pyrazole unit does not participate in a hydrogen bond to the adjacent carboxylate group of the copper atom but donates to the oxygen atom of a water solvent molecule (Fig. 4, Table S3, ESI<sup>†</sup>). This represents the most significant difference to the *sql*-structures where the NH function interacts with the

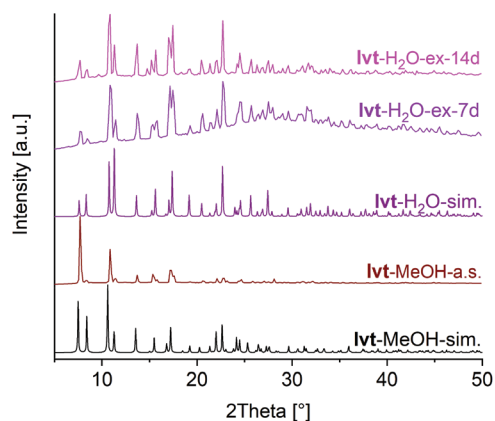


Fig. 3 PXRD patterns of the *lvt*-MeOH-sim., *lvt*-MeOH-a.s., *lvt*-H<sub>2</sub>O-sim. and the different time steps of the exchange after 7 d and 14 d exchange.

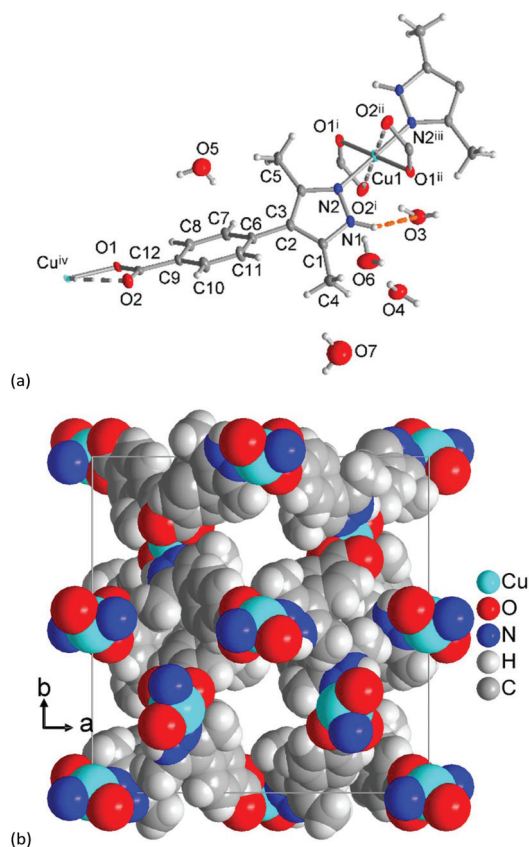


Fig. 4 (a) Metal–ligand coordination in [Cu(Hmpba)<sub>2</sub>] $\cdot$ 9H<sub>2</sub>O, *lvt*-H<sub>2</sub>O (H-bond in orange dashed line. 50% thermal ellipsoids). Symmetry transformations: i =  $y - 3/4, -x + 3/4, -z + 3/4$ ; ii =  $-y + 3/4, x + 1/4, z - 3/4$ ; iii =  $-x, -y + 1, -z$ ; iv =  $y - 1/4, -x + 3/4, z + 3/4$ . (b) Section of the packing diagram in space-filling presentation with water omitted to indicate the potential porosity of the triply-interpenetrated *lvt* network.

carboxylate function of the next layer. The waters of crystallization could be found and refined to be close to 4.5 water molecules, which are distributed over five positions (Fig. 4), corresponding to about nine water molecules per formula unit.

The water substructure in *lvt*-H<sub>2</sub>O is an infinite 3D array of (H<sub>2</sub>O)<sub>20</sub> clusters of *S*<sub>4</sub> symmetry (Fig. 5). The cluster can be

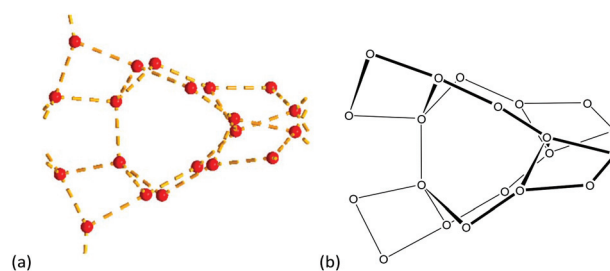


Fig. 5 (a) Structure of the *S*<sub>4</sub>-symmetric (H<sub>2</sub>O)<sub>20</sub> cluster in *lvt*-H<sub>2</sub>O which is extended into a 3D array along the broken-off bonds. Only the O atoms are shown for clarity with the H-bridged O...O contacts (between 2.7–3.1 Å) as yellow dashed lines. (b) Schematic drawing of the (H<sub>2</sub>O)<sub>20</sub> cluster.

described with a central  $(\text{H}_2\text{O})_{12}$  unit composed of four 7-membered rings, onto which four 4-membered rings are annelated (Fig. 5). The H-bridged  $\text{O}\cdots\text{O}$  contacts vary between 2.7 and 3.1 Å. Such higher dimensionality water clusters are rare. A 1D water chain containing  $(\text{H}_2\text{O})_{20}$  was reported in the 2D framework  $[\text{Cd}(\text{phen})_2(\text{male})(\text{H}_2\text{O})]\cdot 9.5\text{H}_2\text{O}$  (male $^{2-}$  = maleate)<sup>45</sup> and a regular pentagonal  $(\text{H}_2\text{O})_{20}$  dodecahedra in the 2D network  $[\text{Ag}_6(\text{Pra}_2\text{biim})_3]\cdot 5.33\text{H}_2\text{O}$  (Pra $_2\text{biim}^{2-}$  = 1,1'-di(propionate)-2,2'-biimidazole)<sup>46</sup>. Theoretical calculations for  $(\text{H}_2\text{O})_{20}$  clusters looked at structures of annelated 4- to 6-membered rings (Fig. S6, ESI†).<sup>47–50</sup> Other large water clusters include, for example, a  $(\text{H}_2\text{O})_{14}$  cluster of  $S_6$  symmetry,<sup>51</sup> a  $(\text{H}_2\text{O})_{12}$ -containing infinite chain,<sup>52</sup> one-dimensional water helices,<sup>53</sup> 2D-water/ice layers with  $(\text{H}_2\text{O})_8$  subunits<sup>54</sup> and a three dimensional open framework.<sup>55</sup>

### Comparison between $\text{sql}[\text{Cu}(\text{Hmpba})_2]$ and $\text{lvt}[\text{Cu}(\text{Hmpba})_2]$ networks

The 2D networks in  $\text{sql}$ -DMF and  $\text{sql}$ -ACN are supramolecular isomers to the 3D frameworks of  $\text{lvt}$ -MeOH<sup>22</sup> and  $\text{lvt}$ -H $_2\text{O}$ . In the  $\text{sql}$  structure the  $\{\text{CuO}_2\text{N}_2\}$  SBUs and the bonding directions of the linkers of a single network all lie in one plane (Fig. 6a). The angle between the  $\{\text{CuO}_2\text{N}_2\}$  planes is 19°. In the

$\text{lvt}$  structures a 3D connectivity is brought about by the tilting of the adjacent  $\{\text{CuO}_2\text{N}_2\}$  planes by 74° (Fig. 6b). The interplanar phenyl–pyrazole angle is similar in the  $\text{sql}$  and the  $\text{lvt}$  networks with 51.7(3)° and 47.6(4)°, respectively.

The difference between the 2D  $\text{sql}$ -networks and the 3D  $\text{lvt}$ -networks can be traced to the templating effect by the solvent of crystallization. The  $\text{sql}$  isomers have DMF and ACN incorporated into the structure. Subsequently, the N–H group seeks an acceptor in the network building blocks and becomes engaged into interlayer N–H $\cdots$ O hydrogen bonds to a carboxylate group from the adjacent layer (Fig. 7a and b). The strong hydrogen-bond acceptors methanol and water in  $\text{lvt}$ -MeOH

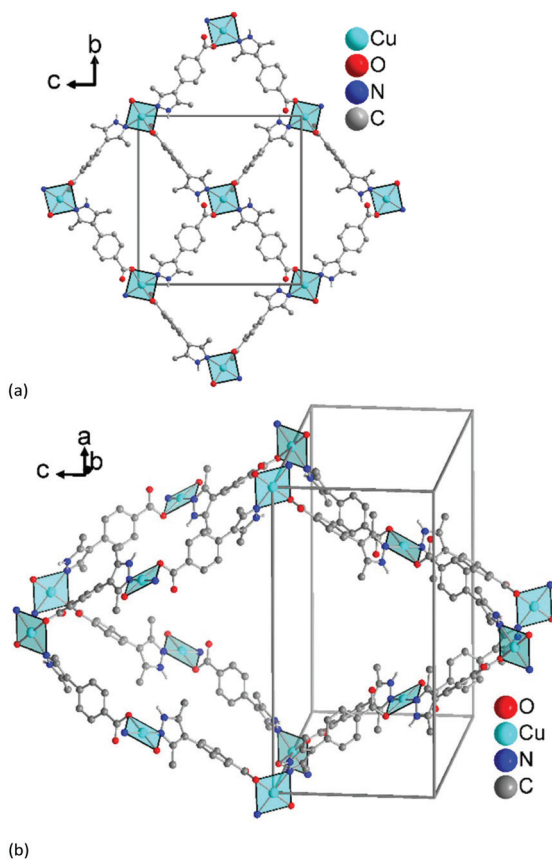


Fig. 6 Single network in (a)  $\text{sql}$ -DMF and in (b)  $\text{lvt}$ -H $_2\text{O}$  to illustrate the different tilting of the adjacent  $\{\text{CuO}_2\text{N}_2\}$  planes. See Fig. S5a and b (ESI†) for the triply-interpenetrating  $\text{lvt}$ -H $_2\text{O}$  network (identical to  $\text{lvt}$ -MeOH<sup>22</sup>).

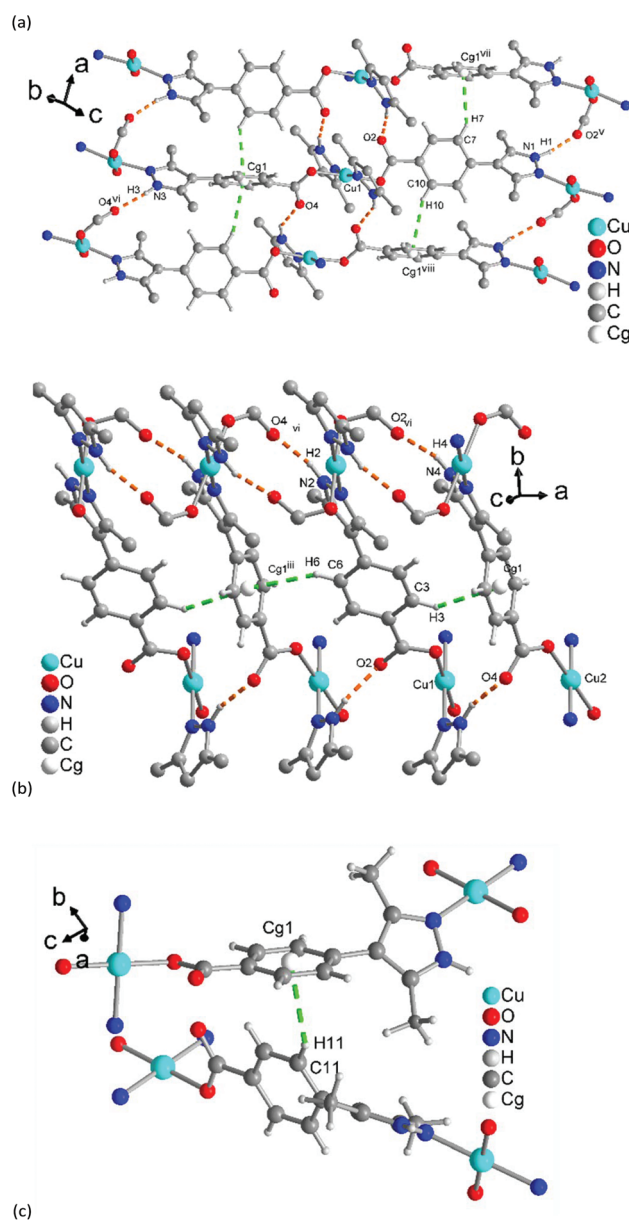


Fig. 7 Representation of the interlayer  $\text{CH}\cdots\pi$  interactions (green-dashed lines) and the  $\text{N}\cdots\text{H}\cdots\text{O}$  hydrogen bonds (orange-dashed lines) in (a)  $\text{sql}$ -DMF and in (b)  $\text{sql}$ -ACN and (c)  $\text{lvt}$ -H $_2\text{O}$ . See Table S3† for details and symmetry transformations.

and **lvt**-H<sub>2</sub>O, respectively, engage the N–H function in a hydrogen bond (Fig. 4a). Thus, the tilting of the {CuO<sub>2</sub>N<sub>2</sub>} SBUs depends on the templating solvent. We note that DMF and ACN are not H-bond donors but are H-bond acceptors, albeit being weaker than water and methanol. Still their H-bond acceptor character is apparently not sufficient to engage the N–H function in a hydrogen bond in the absence of an H-bond donor capability which may be needed to “anchor” the templating solvent in this position.

### Porosity and gas sorption studies

In the work of Richardson and co-workers there was no indication that the compound **lvt**-MeOH and the other reported 3D-**dia** and 2D-**sql** [M(Hmpba)<sub>2</sub>] frameworks could be activated for gas sorption studies.<sup>22</sup> The eclipsed layer stacking in the **sql**-DMF and **sql**-ACN with continuous channel formation (Fig. 2) seemed, however, promising to achieve a permanently porous structure. The activation of the materials was carried by heating **sql**-DMF and **lvt**-MeOH to 160 °C and **sql**-ACN to 110 °C and verified by TGA (Fig. S7–S10, ESI†). While the non-activated **sql** compounds still showed a mass loss due to solvent in the expected temperature range, the activated materials did not exhibit any mass loss up to 300 °C, hence DMF and ACN were completely removed from **sql**-DMF and **sql**-ACN, respectively. After 300 °C decomposition occurred with an abrupt mass loss up to 350 °C of ~30 wt% for **sql**-DMF-act. and ~40 wt% for **sql**-DMF-act. The TGA of the as synthesized **lvt**-MeOH and **lvt**-H<sub>2</sub>O compounds both showed a mass loss of 21% up to ~130 °C, which can be attributed to the loss of 4MeOH + 0.5H<sub>2</sub>O or 7.5H<sub>2</sub>O molecules, respectively, with retention of 1.5H<sub>2</sub>O in the activated structure. The TGA of the activated compound **lvt**-MeOH (**lvt**-MeOH-act.) also shows a mass loss of 4–7%, which indicates the strong hygroscopic nature of the compound during the sample preparation (Fig. S10, ESI†). It follows that compound **lvt**-MeOH-act. still contained 1.5 water molecules above 150 °C and up to 250 °C as was authenticated by Richardson and co-workers with single-crystal X-ray diffraction (compound **8-dry** in ref. 22). Consequently, **lvt**-MeOH-act. had a formula of [Cu(Hmpba)<sub>2</sub>]<sub>2</sub>·1.5H<sub>2</sub>O and was used for the gas sorption measurements. Above 250 °C **lvt**-MeOH and **lvt**-MeOH-act. decomposed.

The experimental PXRD patterns from the activated **sql**-structures (**sql**-DMF-act.; **sql**-ACN-act.) show preservation of crystallinity: the simulated diffractograms from the X-ray structures, where the solvent of crystallization had been removed, match well with the experimental ones (Fig. 8). For the activated **lvt**-MeOH structure the experimental PXRD pattern matches well with the experimental PXRD pattern of the air-dried sample of **lvt**-MeOH reported by Richardson and co-workers (compound **8-dry** in ref. 22) that still contained 1.5 water molecules (Fig. S2c, ESI†).<sup>22</sup>

CO<sub>2</sub> and CH<sub>4</sub> gas sorption studies were performed for the activated **sql**- and **lvt**-networks (Fig. 9, Fig. S15, ESI†). The N<sub>2</sub> gas adsorption was negligible at 77 K (Fig. S12, ESI†). We justify this with the small pore openings of 5 to 6.8 Å (see above) of these networks with possible pore blocking and

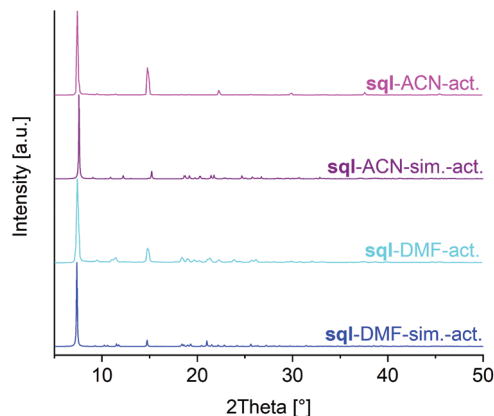


**Fig. 8** PXRD patterns of the activated (act.) **sql**-DMF and **sql**-ACN and their simulated PXRD patterns based on the crystal structures with solvent of crystallization removed (sim.-act.). See Fig. S2a and b, ESI,† for the comparison between the PXRD patterns of the activated structures and the simulations based on the solvent-containing crystal structures.

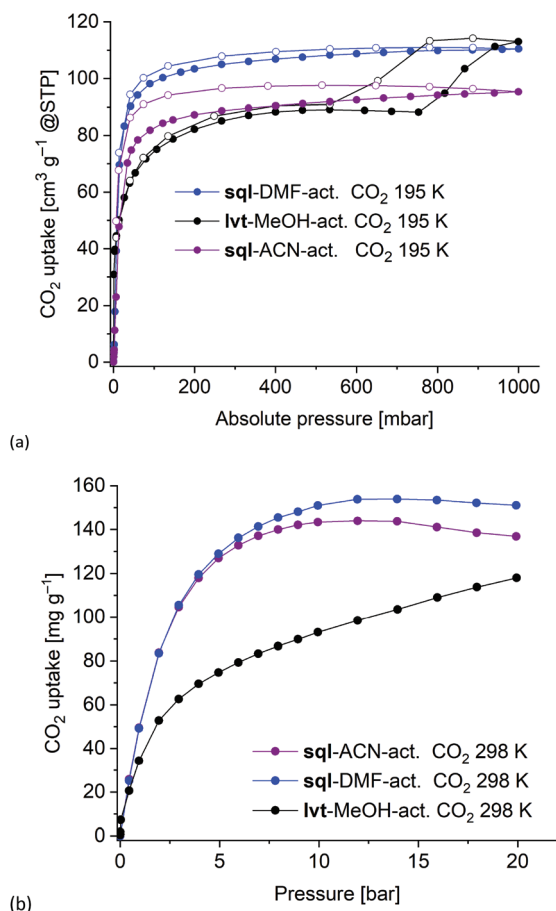


**Fig. 9** (a) Low-pressure CO<sub>2</sub> sorption isotherms of **lvt**-MeOH-act., **sql**-DMF-act. and **sql**-ACN-act. at 195 K with the adsorption points as filled symbols and the desorption points as open symbols. (b) High-pressure CO<sub>2</sub> adsorption isotherms of **lvt**-MeOH-act., **sql**-DMF-act. and **sql**-ACN-act. at 298 K.

structure rearrangement at the pore mouths after removal of the solvent molecules. The diffusion of N<sub>2</sub> molecules with the kinetic diameter of N<sub>2</sub> 3.6 Å at cryogenic temperature of 77 K into small pores is very slow, while kinetic inhibition is lower in the case of CO<sub>2</sub> and CH<sub>4</sub> sorption at 195 K to near room temperature (kinetic diameters 3.3 and 3.76 Å, respectively).

CO<sub>2</sub> adsorption was measured volumetrically at different temperatures at pressures up to 1 bar (Fig. 9a, Fig. S15, ESI†) and gravimetrically at 298 K and up to 20 bar (Fig. 9b). At low pressure all the three activated materials exhibit a steep CO<sub>2</sub> uptake at 195 K due to strong adsorbent-adsorbate interactions in narrow micropores. The low-pressure adsorption curvature for the **sql** nets at 195 K (Fig. 9a) is akin to a Type I isotherm, yet there is a noteworthy hysteresis.<sup>56</sup> The adsorption curvature for **lvt**-MeOH-act. at 195 K could be viewed as initially a Type Ib isotherm turning into a Type IV with its typical feature of a saturation plateau and a hysteresis (here of H2b). A Type H2b hysteresis is associated with pore blocking. Type Ib isotherms are found for materials with wider micropores and narrow mesopores and Type IV isotherms are typical for mesoporous adsorbents.<sup>56</sup> Alternatively, the stepped CO<sub>2</sub> isotherm for the **lvt**-network could be due to a pore opening effect at around 750 mbar (Fig. 9a, Fig. S13, ESI†).

It is noteworthy that, **lvt**-MeOH-act. does not show the uptake step, which was observed at 195 K, when CO<sub>2</sub> adsorption was measured at 273 and 293 K (Fig. S15a, ESI†). This

missing uptake step speaks for a pore opening effect at 195 K at 750 mbar (Fig. 9a). Based on the CO<sub>2</sub> saturation pressure of 1.00 bar at 195 K or a relative pressure of  $P/P_0 = 0.75$ , at 293 K or 298 K the gate opening at the same relative pressure would be expected around 43 bar or 48 bar, respectively. Consequently, a volumetric CO<sub>2</sub> measurement at 293 K up to 1 bar (with  $P/P_0 = 0.017$ ) or a gravimetric high-pressure adsorption at 298 K up to 20 bar ( $P/P_0 = 0.31$ ) does not yet induce the gate opening (Fig. 9b).

The CO<sub>2</sub> sorption data was used to derive the pore volume and pore-size distribution (Table 1, Fig. S14, ESI†) and Langmuir surface area for the activated materials. The lower CO<sub>2</sub> uptake of **sql**-ACN-act. (90 cm<sup>3</sup> g<sup>-1</sup>) versus **sql**-DMF-act. (111 cm<sup>3</sup> g<sup>-1</sup>, both at 1 bar) reflects the narrower pores and lower pore volume seen in the X-ray structures due to the different layer packing (Fig. 2). The **lvt**-network does not reach a plateau in high-pressure CO<sub>2</sub> sorption, but a pore volume of 0.17 cm<sup>3</sup> g<sup>-1</sup> at 20 bar was derived under the assumption of the validity of the Gurvich-rule.<sup>57</sup>

The calculated pore volumes from the volumetric low-pressure and gravimetric high-pressure sorption data are in a good agreement. The pore volumes calculated from the 195 K saturation uptakes for the **sql**-networks are lower than the calculated pore volumes from the X-ray structures. This can be expected as very narrow pore regions (*cf.* Fig. 2) cannot be accessed by CO<sub>2</sub> with its kinetic diameter of 3.3 Å, while

**Table 1** Gas sorption and porosity characteristics

	Uptake		Pore volume <sup>a</sup> [cm <sup>3</sup> g <sup>-1</sup> ]	Langmuir surface area [m <sup>2</sup> g <sup>-1</sup> ]	$\Delta H_{\text{ads}}^{\circ}$ [kJ mol <sup>-1</sup> ] CO <sub>2</sub>	$\Delta H_{\text{ads}}^{\circ}$ [kJ mol <sup>-1</sup> ] CH <sub>4</sub>
	[cm <sup>3</sup> g <sup>-1</sup> ]	[mmol g <sup>-1</sup> ]				
<b>sql</b> -DMF-act.						
CO <sub>2</sub> , 195 K, 1.0 bar	111	4.90	0.26 <sup>b</sup> ; 0.28 <sup>c</sup>	516	-23	
CO <sub>2</sub> , 273 K, 1.0 bar	60	1.37	0.20 <sup>d</sup>			
CO <sub>2</sub> , 293 K, 1.0 bar	33	0.76	0.22 <sup>d</sup>			
CO <sub>2</sub> , 298 K, 20 bar	0.154 g g <sup>-1 e</sup>	3.50				
CH <sub>4</sub> , 273 K, 1.0 bar	27	1.20				-13
CH <sub>4</sub> , 293 K, 1.0 bar	20	0.87				
<b>sql</b> -ACN-act.						
CO <sub>2</sub> , 195 K, 1.0 bar	90	4.00	0.23 <sup>b</sup> ; 0.26 <sup>c</sup>	453	-22	
CO <sub>2</sub> , 273 K, 1.0 bar	60	1.36	0.16 <sup>d</sup>			
CO <sub>2</sub> , 293 K, 1.0 bar	34	0.78	0.20 <sup>d</sup>			
CO <sub>2</sub> , 298 K, 20 bar	0.144 g g <sup>-1 e</sup>	3.30				
CH <sub>4</sub> , 273 K, 1.0 bar	22	1.00				-15
CH <sub>4</sub> , 293 K, 1.0 bar	15	0.67				
<b>lvt</b> -MeOH-act.						
CO <sub>2</sub> , 195 K	0.75 bar: 88 1.0 bar: 113	0.75 bar: 3.90 1.0 bar: 5.00	0.25 <sup>b</sup> ; 0.33 <sup>c</sup>	407		
CO <sub>2</sub> , 298 K, 20 bar	0.124 g g <sup>-1 e</sup>	2.80	0.16 <sup>d</sup>			
CO <sub>2</sub> , 273 K, 1.0 bar	48	1.09	0.21 <sup>d</sup>		-41	
CO <sub>2</sub> , 293 K, 1.0 bar	31	0.73				
CH <sub>4</sub> , 273 K, 1.0 bar	10	0.45				-26
CH <sub>4</sub> , 293 K, 1.0 bar	6	0.25				

<sup>a</sup> Specific pore volume calculated according to  $(\text{SAV} \times N_A)/(Z \times M_{\text{asym unit}})$  or  $(\text{void volume} \times N_A)/(Z \times M_{\text{asym unit}})$ ;  $N_A$  = Avogadro's constant,  $6.022 \times 10^{23} \text{ mol}^{-1}$ ,  $Z$  = number of asymmetric formula units,  $M_{\text{asym unit}}$  = molecular weight of asymmetric formula unit [in g mol<sup>-1</sup>]. The potential solvent area volume (SAV) or void volume [in Å<sup>3</sup>] was calculated from. <sup>b</sup> By the program Mercury<sup>33</sup> with a probe radius of 1.2 Å, grid spacing of 0.7 Å; values calculated using 'contact surface'. <sup>c</sup> From the crystal structures, where the solvent of crystallization had been removed, with PLATON for Windows ('calc. void' calculation)<sup>37</sup>. <sup>d</sup> Under the assumption of the validity of the Gurvich rule according to (specific amount adsorbed)/(density of liquid adsorbate) with the CO<sub>2</sub> saturation pressure at 298 K of 64.3 bar, at 293 K of 57.3 bar and at 195 K of 1.00 bar with  $\rho_{\text{CO}_2}(195 \text{ K}) = 1.08 \text{ g cm}^{-3}$  and  $\rho_{\text{CO}_2}(298 \text{ K}) = 0.712 \text{ g cm}^{-3}$ .<sup>57</sup> <sup>e</sup> The unit g g<sup>-1</sup> is due to the gravimetric uptake in the high-pressure adsorption.

PLATON<sup>37</sup> uses a probe sphere of 1.2 Å radius rolling over the Connolly surface.

As expected, the uptake of the slightly larger non-polar gas CH<sub>4</sub> is significantly lower than for CO<sub>2</sub>. Furthermore, **lvt**-MeOH-act. adsorbs notably less CH<sub>4</sub> than **sql**-DMF-act. and **sql**-ACN-act. (Fig. S15b†). The determined CO<sub>2</sub>:CH<sub>4</sub> selectivity by the Henry plots of the adsorption isotherms is slightly higher for the **lvt**-network than for the **sql**-networks (Fig. S19, Table S5, ESI†). This can be reasoned by the residual water content in the **lvt**-network, which disfavors the uptake of CH<sub>4</sub>. The higher selectivity for CO<sub>2</sub> for the **sql**-ACN-act. network over **sql**-DMF-act. can be traced to the smaller limiting pore diameters in the former which better discriminates between the smaller CO<sub>2</sub> and larger CH<sub>4</sub> gas molecules.

The isosteric enthalpy of adsorption at zero coverage,  $\Delta H_{\text{ads}}^{\circ}$  for CO<sub>2</sub> and CH<sub>4</sub> from adsorption isotherms at 273–293 K (Fig. S15, ESI†) was calculated with the virial fit method (Table 1, Fig. S17 and S18, ESI†).<sup>58</sup> As expected, the values of the isosteric enthalpy of adsorption for CO<sub>2</sub> are significantly higher than for CH<sub>4</sub> for all three materials. At the same time, the magnitude of the isosteric enthalpy for CO<sub>2</sub> for the **lvt**-MeOH network is relatively high with  $-41 \text{ kJ mol}^{-1}$  compared to other MOFs (typical range between  $21\text{--}39 \text{ kJ mol}^{-1}$ ).<sup>59,60</sup> The still present water molecule in **lvt**-MeOH is seen as the basis for the high isosteric enthalpy. In contrast,  $\Delta H_{\text{ads}}^{\circ}$  for CO<sub>2</sub> in both **sql**-networks is at the lower end of the typical range.<sup>59,60</sup>

To classify the **sql** and **lvt** structures in terms of hydrophobicity and hydrophilicity, water (Fig. 10) and ethanol sorption measurements (Fig. S21, ESI†) were carried out and the Henry constants were determined (Table S6, Fig. S20a, ESI†). The activated **sql**-DMF network (**sql**-DMF-act.) was used exemplarily because of the better pore accessibility over the **sql**-ACN network (which was evident from CO<sub>2</sub> sorption).

For **sql**-DMF-act. the water uptake at high  $P/P_0 > 0.4$  and a Henry constant value in the order of  $10^{-7} \text{ g mol}^{-1} \text{ Pa}^{-1}$  corresponds to a hydrophobic character of the pores.<sup>61</sup> On the other hand, the early water uptake below  $P/P_0 = 0.1$  and a Henry constant of  $10^{-5} \text{ g mol}^{-1} \text{ Pa}^{-1}$  for **lvt**-MeOH-act. indicates a rather hydrophilic material.<sup>62,63</sup> At the adsorption maximum ( $P/P_0 =$

0.9) the **lvt**-MeOH-act. structure has adsorbed 2.8 water molecules per formula unit ( $5.7 \text{ mmol g}^{-1}$ ). Together with the residual 1.5 water molecules, the structure then contains 4.3 water molecules per formula unit. This agrees well with the 4.5 water molecules found in the crystal structure of the water exchanged **lvt**-H<sub>2</sub>O material.

The isosteric enthalpy of water adsorption for the **sql**-DMF-act. material increases with the water uptake from  $-32$  to  $-50 \text{ kJ mol}^{-1}$  (Fig. S20b†), which is only slightly above the evaporation enthalpy of water ( $44 \text{ kJ mol}^{-1}$ ).<sup>64</sup> In contrast,  $\Delta H_{\text{ads}}$  for the activated **lvt**-MeOH increases from  $-41$  to  $-64 \text{ kJ mol}^{-1}$ , which underlines the hydrophilicity of the material. For the initial increase in  $\Delta H_{\text{ads}}$  for the hydrophobic **sql**-DMF a framework flexibility or phase change may be proposed, through which anchor points could be formed for the subsequent (increasing) adsorption of water. Such a flexibility or phase change induced by the first water molecules at high  $P/P_0$  in **sql**-DMF could make the  $-\text{NH}$  groups of the Hmpba<sup>-</sup> ligand available as H-bond donor sites. For **lvt**-MeOH the initial increase in  $\Delta H_{\text{ads}}$  is proposed to be due to a similar gate-opening effect as for the CO<sub>2</sub> adsorption. The isotherm of the ethanol sorption at 293 K (Fig. S21, ESI†) corroborates the flexibility of the **lvt**-network by showing a sudden opening at  $P/P_0 \approx 0.1$  with a Type F-II isotherm.<sup>65</sup> For the **sql**-network the ethanol adsorption isotherm at 293 K shows a gradual increase.

## Conclusion

In this contribution we present two new microporous 2D metal–organic frameworks **sql**-[Cu(Hmpba)<sub>2</sub>] $\cdot$ *x*DMF and **sql**-[Cu(Hmpba)<sub>2</sub>] $\cdot$ 2ACN which are based on the linear, bifunctional 4-(3,5-dimethyl-1*H*-pyrazol-4-yl)benzoate linker in its monodeprotonated form Hmpba<sup>-</sup>. The microporous character of the two activated MOFs was demonstrated by CO<sub>2</sub> and CH<sub>4</sub> sorption. The 2D MOFs are supramolecular isomers of already known 3D **lvt**-Cu frameworks [Cu(Hmpba)<sub>2</sub>] $\cdot$ L<sub>solv</sub>. Through a methanol-to-water solvent exchange we could derive from **lvt**-[Cu(Hmpba)<sub>2</sub>] $\cdot$ 4MeOH $\cdot$ 1H<sub>2</sub>O at the new all-water isomer 3D **lvt**-[Cu(Hmpba)<sub>2</sub>] $\cdot$ 9H<sub>2</sub>O, with a water substructure of a 3D array of *S*<sub>4</sub>-symmetric (H<sub>2</sub>O)<sub>20</sub> clusters. The potential porosity of the **lvt**-[Cu(Hmpba)<sub>2</sub>] isomers had not been described before and here we showed for the first time that the 3D network **lvt**-[Cu(Hmpba)<sub>2</sub>] $\cdot$ 4MeOH $\cdot$ 1H<sub>2</sub>O could be activated for CO<sub>2</sub> and CH<sub>4</sub> adsorption in with it displays a gate-opening effect. A crucial structural difference between the supramolecular **sql**- and **lvt**-[Cu(Hmpba)<sub>2</sub>] isomers is the engagement of the  $-\text{NH}$  group of the pyrazolyl moiety in inter-network H-bonding in the former and in crystal-water H-bonding in the latter. This difference then leads to a hydrophobic character of the **sql**-materials and a hydrophilic **lvt**-network, which was demonstrated here by water and ethanol sorption through their isotherm shape, relative uptake pressure and isosteric enthalpy of adsorption.

The [M(Hmpba)<sub>2</sub>]-solvent materials reported here are relatively rare examples of supramolecular framework isomers

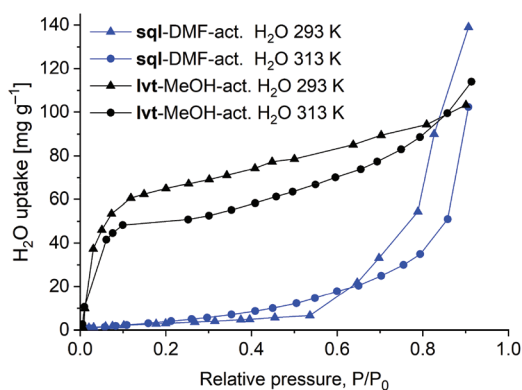


Fig. 10 Water adsorption isotherms of **sql**-DMF-act. and **lvt**-MeOH-act. at 293 K and at 313 K.

where subtle changes in H-bonding around metal centers result in substantial changes in structure and sorption properties. The combination of the heteroditopic approach in combination with different synthetic conditions (solvent templating) are the reason for these different isomers.

## Conflicts of interest

There are no conflicts to declare.

## Acknowledgements

The authors thank Dr Christian Heering for the preparation of the water structure, Mrs Birgit Tommes for carrying out the FT-IR experiments and Dr Ishtvan Boldog for the introduction to the topic of bifunctional pyrazolate-carboxylate MOFs, for supervision of students and for the numerous advices regarding the scientific work in general and in manuscript writing.

## Notes and references

- 1 C. Janiak and J. K. Vieth, MOFs, *New J. Chem.*, 2010, **34**, 2366–2388.
- 2 (a) R. B. Getman, Y.-S. Bae, C. E. Wilmer and R. Q. Snurr, *Chem. Rev.*, 2012, **112**, 703–723; (b) K. Adil, Y. Belmabkhout, R. S. Pillai, A. Cadiau, P. M. Bhatt, A. H. Assen, G. Maurin and M. Eddaoudi, *Chem. Soc. Rev.*, 2017, **46**, 3402–3430.
- 3 S. M. J. Rogge, A. Bavykina, J. Hajek, H. Garcia, A. I. Olivoso-Suarez, A. Sepúlveda-Escribano, A. Vimont, G. Clet, P. Bazin, F. Kapteijn, M. Daturi, E. V. Ramos-Fernandez, F. X. Llabrés i Xamena, V. Van Speybroeck and J. Gascon, *Chem. Soc. Rev.*, 2017, **46**, 3134–3184.
- 4 R. Medishetty, J. K. Zareba, D. Mayer, M. Samoc and R. A. Fischer, *Chem. Soc. Rev.*, 2017, **46**, 4976–5004.
- 5 G. Mínguez Espallargas and E. Coronado, *Chem. Soc. Rev.*, 2018, **47**, 533–557.
- 6 W. P. Lustig, S. Mukherjee, N. D. Rudd, A. V. Desai, J. Li and S. K. Ghosh, *Chem. Soc. Rev.*, 2017, **46**, 3242–3285.
- 7 X. Lian, Y. Fang, E. Joseph, Q. Wang, J. Li, S. Banerjee, C. Lollar, X. Wang and H.-C. Zhou, *Chem. Soc. Rev.*, 2017, **46**, 3386–3401.
- 8 J. Dechnik, C. J. Sumby and C. Janiak, *Cryst. Growth Des.*, 2017, **17**, 4467–4488.
- 9 J. Dechnik, J. Gascon, C. J. Doonan, C. Janiak and C. J. Sumby, *Angew. Chem., Int. Ed.*, 2017, **56**, 9292–9310.
- 10 F. ZareKarizi, M. Joharian and A. Morsali, *J. Mater. Chem. A*, 2018, **6**, 19288–19329.
- 11 L. Hou, Y.-Y. Lin and X.-M. Chen, *Inorg. Chem.*, 2008, **47**, 1346–1351.
- 12 L.-N. Jia, Y. Zhao, L. Hou, L. Cui, H.-H. Wang and Y.-Y. Wang, *J. Solid State Chem.*, 2014, **210**, 251–255.
- 13 G. Mehlana, V. Chitsa and T. Mugadza, *RSC Adv.*, 2015, **5**, 88218–88233.
- 14 P. Pachfule, B. Garai and R. Banerjee, *Inorg. Chem.*, 2016, **55**, 7200–7205.
- 15 C. Heering, B. Francis, B. Nateghi, G. Makhoulfi, S. Lüdeke and C. Janiak, *CrystEngComm*, 2016, **18**, 5209–5223.
- 16 M. Deng, Y. Liang, B. Xing, Z. Chen, Y. Zhou, X. Liu, B. Yue and H. He, *Chem. – Eur. J.*, 2011, **17**, 10323–10328.
- 17 C. Montoro, F. Linares, E. Quartapelle Procopio, I. Senkovska, S. Kaskel, S. Galli, N. Masciocchi, E. Barea and J. A. R. Navarro, *J. Am. Chem. Soc.*, 2011, **133**, 11888–11891.
- 18 C. Heering, I. Boldog, V. Vasylyeva, J. Sanchiz and C. Janiak, *CrystEngComm*, 2013, **15**, 9757–9768.
- 19 B. Nateghi and C. Janiak, *Z. Naturforsch. B*, 2019, **74**, 891–899.
- 20 C.-T. He, J.-Y. Tian, S.-Y. Liu, G. Ouyang, J.-P. Zhang and X.-M. Chen, *Chem. Sci.*, 2013, **4**, 351–356.
- 21 B. Tu, Q. Pang, D. Wu, Y. Song, L. Weng and Q. Li, *J. Am. Chem. Soc.*, 2014, **136**, 14465–14471.
- 22 M. R. Bryant, A. D. Burrows, C. M. Fitchett, C. S. Hawes, S. O. Hunter, L. L. Keenan, D. J. Kelly, P. E. Kruger, M. F. Mahon and C. Richardson, *Dalton Trans.*, 2015, **44**, 9269–9280.
- 23 X.-L. Qi, C. Zhang, B.-Y. Wang, W. Xue, C.-T. He, S.-Y. Liu, W.-X. Zhang and W.-M. Chen, *CrystEngComm*, 2013, **15**, 9530–9536.
- 24 S. Millan, B. Gil-Hernandes, E. Milles, S. Gökpınar, G. Makloufi, A. Schmitz, C. Schlüssener and C. Janiak, *Dalton Trans.*, 2019, **48**, 8057–8067.
- 25 T. A. Makal, A. A. Yakovenko and H.-C. Zhou, *J. Phys. Chem. Lett.*, 2011, **2**, 1682–1689.
- 26 B. Moulton and M. J. Zaworotko, *Chem. Rev.*, 2001, **101**, 1629–1658.
- 27 P. M. Forster, A. R. Burbank, C. Livage, G. Férey and A. K. Cheetham, *Chem. Commun.*, 2004, 368–369.
- 28 J.-P. Zhang, X. C. Huang and X.-M. Chen, *Chem. Soc. Rev.*, 2009, **38**, 2385–2396.
- 29 C.-T. He, P.-Q. Liao, D.-D. Zhou, B.-Y. Wang, W.-X. Zhang, J.-P. Zhang and X.-M. Chen, *Chem. Sci.*, 2014, **5**, 4755–4762.
- 30 (a) O. D. Friedrichs, M. O’Keeffe and O. M. Yaghi, *Acta Crystallogr., Sect. A: Found. Crystallogr.*, 2003, **59**, 515–525; (b) M. O’Keeffe, M. A. Peskov, S. J. Ramsden and O. M. Yaghi, *Acc. Chem. Res.*, 2008, **41**, 1782–1789; (c) V. Alexandrov, V. A. Blatov and D. M. Proserpio, *Acta Crystallogr., Sect. A: Found. Crystallogr.*, 2012, **68**, 484–493.
- 31 Z.-M. Ye, C.-T. He, Y.-T. Xu, R. Krishna, Y. Xie, D.-D. Zhou, H.-L. Zhou, J.-P. Zhang and X.-M. Chen, *Cryst. Growth Des.*, 2017, **17**, 2166–2171.
- 32 G. Mehlana, C. Wilkinson, C. N. Dzesse T., G. Ramon and S. A. Bourne, *Cryst. Growth Des.*, 2017, **17**, 6445–6454.
- 33 C. F. Macrae, I. J. Bruno, J. A. Chisholm, P. R. Edgington, P. McCabe, E. Pidcock, L. Rodriguez-Monge, R. Taylor, J. van de Streek and P. A. Wood, *J. Appl. Crystallogr.*, 2008, **41**, 466–470.
- 34 Apex2 - Data Collection Program for the CCD Area-Detector System; SAINT - Data Reduction and Frame Integration

- Program for the CCD Area-Detector System*. Bruker Analytical X-ray Systems, Madison, Wisconsin, USA, 1997–2014.
- 35 (a) G. Sheldrick, *Program SADABS: Area-detector absorption correction*, University of Göttingen, Germany, 1996–2014; (b) L. Krause, R. Herbst-Irmer, G. M. Sheldrick and D. Stalke, *J. Appl. Crystallogr.*, 2015, **48**, 3–10.
- 36 G. M. Sheldrick, *Acta Crystallogr., Sect. A: Found. Adv.*, 2015, **e71**, 3–8.
- 37 A. L. Spek, *Structure Validation in Chemical Crystallography*, *Acta Crystallogr., Sect. D: Biol. Crystallogr.*, 2009, **65**, 148–155; A. L. Spek, *PLATON – A Multipurpose Crystallographic Tool*, Utrecht University, Utrecht, The Netherlands, 2008; Windows implementation; L. J. Farrugia, Version 280317, University of Glasgow, Scotland, 2020.
- 38 (a) M. Nishio, *Phys. Chem. Chem. Phys.*, 2011, **13**, 13873–13900; M. Nishio, Y. Umezawa, K. Honda, S. Tsuboyama and H. Suezawa, *CrystEngComm*, 2009, **11**, 1757–1788; (b) M. Nishio, *CrystEngComm*, 2004, **6**, 130–158; (c) C. Janiak, S. Temizdemir, S. Dechert, W. Deck, F. Girgsdies, J. Heinze, M. J. Kolm, T. G. Scharmann and O. M. Zipffel, *Eur. J. Inorg. Chem.*, 2000, 1229–1241; (d) Y. Umezawa, S. Tsuboyama, K. Honda, J. Uzawa and N. Motoshiro, *Bull. Chem. Soc. Jpn.*, 1998, **71**, 1207–1213; (e) M. Nishio, M. Hirota and Y. Umezawa, *The CH/π interaction (evidence, nature and consequences)*, Wiley-VCH, New York, 1998.
- 39 C. Glidewell, J. N. Low, J. M. S. Skale and J. L. Wardell, *Acta Crystallogr., Sect. B: Struct. Sci.*, 2006, **62**, 666–675.
- 40 D. Chen, Y.-J. Liu, Y.-Y. Lin, J.-P. Zhang and X.-M. Chen, *CrystEngComm*, 2011, **13**, 3827–3831.
- 41 F. Jeremias, D. Fröhlich, C. Janiak and S. K. Henninger, *New J. Chem.*, 2014, **38**, 1846–1852.
- 42 M. F. de Lange, K. J. Verouden, T. J. Vlugt, J. Gascon and F. Kapteijn, *Chem. Rev.*, 2015, **115**, 12205–12250.
- 43 D. Fröhlich, E. Pantatosaki, P. D. Kolokathis, K. Markey, H. Reinsch, M. Baumgartner, M. A. van der Veen, D. E. De Vos, N. Stock, G. K. Papadopoulos, S. K. Henninger and C. Janiak, *J. Mater. Chem. A*, 2016, **4**, 11859–11869.
- 44 S. Gökpınar, S.-J. Ernst, E. Hastürk, M. Möllers, I. El Aita, R. Wiedey, N. Tannert, S. Nießing, S. Abdpour, A. Schmitz, J. Quodbach, G. Fuldner, S. K. Henninger and C. Janiak, *Ind. Eng. Chem. Res.*, 2019, **58**, 21493–21503.
- 45 X. Liu, W. C. Lu, C. Z. Wang and K. M. Ho, *Chem. Phys. Lett.*, 2011, **508**, 270–275.
- 46 Y.-G. Sun, F. Ding, X.-F. Gu, W.-Z. Zhang, D.-Z. Wie and E.-J. Gao, *Chin. J. Chem.*, 2008, **26**, 1843–1847.
- 47 G. S. Fanourgakis, E. Aprá and S. S. Xantheas, *J. Chem. Phys.*, 2004, **121**, 2655.
- 48 B. Bandow and B. Hartke, *J. Phys. Chem. A*, 2006, **110**, 5809–5822.
- 49 B. Hartke, *Phys. Chem. Chem. Phys.*, 2003, **5**, 275–284.
- 50 R. L. Sang and L. Xu, *CrystEngComm*, 2010, **12**, 1377–1381.
- 51 F. Zhuge, B. Wu, L. Dong, J. Yang, C. Janiak, N. Tang and X.-J. Yang, *Aust. J. Chem.*, 2010, **63**, 1358–1364.
- 52 Q. Y. Liu and L. Xu, *CrystEngComm*, 2005, **7**, 87–89.
- 53 S.-C. Chen, F. Tian, K.-L. Huang, C.-P. Li, J. Zhong, M.-Y. He, Z.-H. Zhang, H.-N. Wang, M. Du and Q. Chen, *CrystEngComm*, 2014, **16**, 7673–7680.
- 54 C. Janiak, T. G. Scharmann and S. A. Mason, *J. Am. Chem. Soc.*, 2002, **124**, 14010–14011.
- 55 R. Carballo, B. Covelo, C. Lodeiro and E. M. Vázquez-López, *CrystEngComm*, 2005, **7**, 294–296.
- 56 M. Thommes, K. Kaneko, A. V. Neimark, J. P. Olivier, F. Rodriguez-Reinoso, J. Rouquerol and K. S. W. Sing, *Pure Appl. Chem.*, 2015, **87**, 1051–1069.
- 57 L. Gurvich, *J. Soc. Phys.–Chim. Russe*, 1915, **47**, 805–827.
- 58 A. Nuhnen and C. Janiak, *Dalton Trans.*, 2020, **49**, 10295–10307.
- 59 K. Sumida, D. L. Rogow, J. A. Mason, T. M. McDonald, E. D. Bloch, Z. R. Herm, T.-H. Bae and J. R. Long, *Chem. Rev.*, 2012, **112**, 724–781.
- 60 A. Das and D. M. D'Alessandro, *CrystEngComm*, 2015, **17**, 706–718.
- 61 G. Wang, K. Leus, H. S. Jena, C. Krishnaraj, S. Zhao, H. Depauw, N. Tahir, Y.-Y. Liu and P. van der Voort, *J. Mater. Chem. A*, 2018, **6**, 6370–6375.
- 62 S. Dissegna, R. Hardian, K. Epp, G. Kieslich, M.-V. Coulet, P. Llewellyn and R. A. Fischer, *CrystEngComm*, 2017, **19**, 4137–4141.
- 63 J. Canivet, J. Bonnefoy, C. Daniel, A. Legrand, B. Coasne and D. Farrusseng, *New J. Chem.*, 2014, **38**, 3102–3111.
- 64 F. Jeremias, A. Khutia, S. K. Henninger and C. Janiak, *J. Mater. Chem.*, 2012, **22**, 10148–10151.
- 65 Q.-Y. Yang, P. Lama, S. Sen, M. Lusi, K.-J. Chen, W.-Y. Gao, M. Shivanna, T. Pham, N. Hosono, S. Kusaka, J. J. Perry IV, S. Ma, B. Space, L. J. Barbour, S. Kitagawa and M. J. Zaworotko, *Angew. Chem., Int. Ed.*, 2018, **57**, 5684–5689.